Self-Assembled Structure Evolution of Mn—Fe Oxides for High Temperature Thermochemical Energy Storage
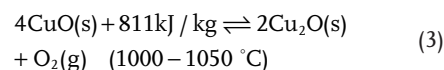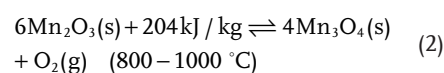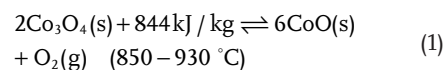
Duo Xiang, Changdong Gu, Haoran Xu, and Gang Xiao*

Thermochemical energy storage (TCES) materials have emerged as a promising alternative to meet the high-temperature energy storage requirements of concentrated solar power plants. However, most of the energy storage materials are facing challenges in redox kinetics and cyclic stability. Iron-doped manganese oxide attracts raising attention due to its non-toxicity, low cost, and high energy capacity over 800 °C. However, there are few investigations on the reversibility enhancement of the redox reaction from the microstructural-evolution-mechanism point of view. Herein, bixbyite-type $(Mn_{0.8}Fe_{0.2})_2O_3$ is synthesized and extruded into honeycomb units, which can maintain an 85% initial capacity after 100 redox cycles. It is also found that a self-assembled core-shell $MnFe_2O_4@Mn_{2.7}Fe_{0.3}O_4$ structure forms during the reduction step, and then transforms into a homogeneous solid solution of $(Mn_{0.8}Fe_{0.2})_2O_3$ in the following oxidation step. During the reduction step, shells are formed spontaneously from the $Mn_{2.7}Fe_{0.3}O_4$ with the $MnFe_2O_4$ as cores due to the lower surface energy, which facilitates the oxygen adsorption and dissociation during subsequent oxidation step. Through the density functional theory calculation, it is revealed that the lower formation energy of oxygen vacancies in the shell contributes to the improvement of oxygen diffusion rate. This study can provide a guideline to design prospective materials for high-temperature TCES.

1. Introduction

Thermochemical energy storage (TCES), based on the energy absorbed and released in reversible thermochemical reactions,[1] is a promising technology to meet the needs of the next-generation concentrated solar power (CSP) plants at high operating temperatures.[2] To simplify the structure and match the operating temperature of the CSP system, multivalent metal oxides with gas-solid reactions are identified as the optimal materials,[3] which cover a range of temperature and

D. Xiang, Dr. H. R. Xu, Prof. G. Xiao
State Key Laboratory of Clean Energy Utilization
College of Energy Engineering
Zhejiang University
Hangzhou, Zhejiang 310027, China
E-mail: xiaogangtianmen@zju.edu.cn
Prof. C. D. Gu
State Key Laboratory of Silicon Materials
College of Materials Science and Engineering
Zhejiang University
Hangzhou, Zhejiang 310027, China

The ORCID identification number(s) for the author(s) of this article can be found under https://doi.org/10.1002/smll.202101524.

provide flexibility to the design of TCES devices.[4–6] In CSP systems, Co_3O_4/CoO, Mn_2O_3/Mn_3O_4, and CuO/Cu_2O are three typical types of metal oxides couples as shown in Equations (1)–(3).[7–9]

$$2Co_3O_4(s) + 844\,kJ\,/\,kg \rightleftharpoons 6CoO(s) + O_2(g) \quad (850-930\ ^{\circ}C) \tag{1}$$

$$6Mn_2O_3(s) + 204\,kJ\,/\,kg \rightleftharpoons 4Mn_3O_4(s) + O_2(g) \quad (800-1000\ ^{\circ}C) \tag{2}$$

$$4CuO(s) + 811\,kJ\,/\,kg \rightleftharpoons 2Cu_2O(s) + O_2(g) \quad (1000-1050\ ^{\circ}C) \tag{3}$$

The Co_3O_4/CoO couple is widely reported[10–16] due to its high energy storage density and completeness in reversible reactions, but the commercial applications are limited by its toxicity and high cost.[17] The CuO/Cu_2O couple suffers from poor oxidation kinetics, because CuO/Cu_2O particles are liable to sintering[18,19] and CuO tends to melt (1077 °C) at reduction temperature. Mn_2O_3/Mn_3O_4 couple is more feasible for thermochemical storage because it is non-toxic, low cost, and has a suitable reaction temperature (800–1000 °C).[4,20–22] The previous researchers have focused more on the reaction kinetics of pure Mn_2O_3/Mn_3O_4 material. Wong[23] first tried to adopt Mn_2O_3/Mn_3O_4 couple for thermochemical storage purposes, but he found that the oxidation reaction of Mn_3O_4 could hardly happen. Carrillo[24] looked into the poor oxidation kinetics of Mn_3O_4 and found it was significantly affected by the morphology feature of the Mn_2O_3, where a small particle size led to slow oxidation rate and high reaction temperature due to the severe particle agglomeration and poor oxygen diffusion. To improve the oxidation rate of manganese oxide, various elements were introduced to change the material properties.[15,25–28] Agrafiotis[5] reported that the addition of Fe_2O_3 could improve both reduction and oxidation rates. The powder was prepared to small-scale foam via the PU foam replica method, both powder and shaped foam of Mn—Fe mixed oxides showed good cyclic stability. Al-Shankiti[20] also found that adding Fe_2O_3 into Mn_2O_3 with a molar ratio of 2:1 exhibited good reaction kinetics. Hlongwa[29] further prepared $LiMn_2O_4$ and $CuMn_2O_4$ to measure their thermochemical capacity, where they found the enthalpies could be 209 and 144 kJ kg^{-1}, respectively. Despite the limited samples showing the positive doping effects, Fe incorporation seems to be a promising solution to improve the oxidation kinetics of Mn_2O_3.

**ADVANCED
SCIENCE NEWS**
www.advancedsciencenews.com

NANO · MICRO
small
www.small-journal.com

However, its mechanism is still ambiguous, because there is a wide spectrum of opinions from the kinetic perspective on iron-doped manganese oxides.[21,26,30] Moreover, previous works focused more on thermogravimetric analysis, which has little significance for practical applications.

In summary, the foremost problems of Mn_2O_3/Mn_3O_4 system are the slow oxidation rate and the poor cyclic stability. With the hope to improve its performance by doping Fe element, a clear mechanism from the microstructure viewpoint is urgently needed to rationally design and optimize advanced materials for practical thermochemical storage applications.

In this work, we synthesize bixbyite-type $(Mn_{0.8}Fe_{0.2})_2O_3$ and extrude it into honeycomb units for TCES. The microstructural evolution between homogeneous $(Mn_{0.8}Fe_{0.2})_2O_3$ and core-shell $MnFe_2O_4@Mn_{2.7}Fe_{0.3}O_4$ structure is observed via experimental characterization, providing fundamental insights into the redox mechanism of $(Mn_{0.8}Fe_{0.2})_2O_3$. DFT calculations are further performed to verify the enhancement of oxygen diffusion in both core and shell during the oxidation reaction. The presented results provide a guideline to rationally design advanced materials for solar TCES.

2. Results and Discussion

2.1. Energy Storage Performance

The feasibility of solid-gas reaction for the thermochemical storage is contingent upon the satisfactory performance of redox reaction rate and cyclic stability. Detailed characterizations of scanning electron microscope (SEM) and X-ray diffraction (XRD) for prepared powders are shown in Figure S1, Supporting Information. Four kinds of $(Mn_{1-\delta}Fe_\delta)_2O_3$ (δ = 0.1, 0.2, 0.3, 0.4) and Mn_2O_3 (10 mg for each kind) are tested and compared via TGA, as shown in Figure. S2, Supporting Information. Among these, $(Mn_{0.8}Fe_{0.2})_2O_3$ is the optimal one based on the analysis of the reaction rate, the mass change fraction, and the difference of starting temperatures between reduction and oxidation reactions.[30] Detailed kinetics of different components are discussed in Supporting Information.

DSC is adopted to measure the enthalpy of $(Mn_{0.8}Fe_{0.2})_2O_3$ in the synthetic air, as shown in Figure S3, Supporting Information. The endothermic and exothermic peaks are observed distinctly, corresponding to the reduction and oxidation reactions respectively. Its enthalpy changes in the reduction and the oxidation reactions are 171.95 and 201.56 J g^{-1}, respectively. The relative lower reduction enthalpy is probably caused by the instrument fluctuation error, and the oxidation enthalpy value is close to the value of Mn_2O_3 (202 J g^{-1}).

Long-term stability is the key criteria for the practical application of the material. 10 cycles of TGA test of the $(Mn_{0.8}Fe_{0.2})_2O_3$ are carried out to investigate the influence of sintering as shown in Figure S4, Supporting Information. $(Mn_{0.8}Fe_{0.2})_2O_3$ presents a high stability after 10 cycles with a remained capacity to be 96.69%. The curve has near-vertical slopes at each reduction and oxidation processes, indicating the reaction rate stabilize at high speeds. A rapid reaction rate shortens the time needed for the charge/discharge of the CSP and fulfills the requirement of dynamic adjustments in the practical storage uses.

The reaction activity and cyclic stability of four honeycomb $(Mn_{0.8}Fe_{0.2})_2O_3$ units with a total weight of 110 g are further investigated as shown in **Figure 1**. The honeycombs are heated from ambient temperature to 1100 °C with a 10 °C min^{-1} ramp rate, stay for 90 mins, then cooled down to 700 °C with a 10 °C min^{-1} ramp rate and stay again for 90 mins to ensure a complete reaction as shown in Figure 1a. Plateaus occur at about 990 and 850 °C and last for about 10 mins despite the rapid release and consumption of oxygen in the heating and cooling processes, indicating a stable operating temperature can be maintained by the material regardless of the temperature difference with the wall. This is very important in strong solar radiation situations, where excessive heat can be effectively stored by the material when keeping a constant temperature. More details about the conversion rate of the honeycomb $(Mn_{0.8}Fe_{0.2})_2O_3$ in oxidation and reaction processes are shown in Figure 1b. The range with conversion ratios between 0.2 to 0.8 is regarded as the rapid-reaction region, where the temperature is almost unchanged. The slope in oxidation is not as steep as that in reduction, indicating a slower reaction rate. As shown in Figure 1c, the time-lapse in reduction and oxidation processes are 23 and 28 mins, respectively, which is much larger than that in the TGA test due to the heat transfer limitation in large quantities. The reaction rates of the two reactions are compared by oxygen changing amounts per unit material mass, as shown in Figure 1d. Reduction process took place in a slimmer temperature range and faster rate compared with the oxidation process due to the higher reaction temperature. Different operating temperatures between the reduction and oxidation process will lead to the loss of heat yield, promoting the oxidation temperature is still needed to improve the heat yield in TCES.

The results of the preliminary experiment have shown that the honeycomb $(Mn_{0.8}Fe_{0.2})_2O_3$ has excellent performance for TCES in the first reaction cycle. Long-term tests of 100 cycles are thus performed to exam its stability as shown in **Figure 2**. The effective mass that participates in the reaction is calculated by transferring the oxygen reactant with stoichiometric parameters, and the conversion rate can be acquired when the effective mass is divided by total mass. This rate keeps at a high level in the first fifteen cycles with the eighth cycle approaching 99.4% of the full capacity. After 100 cycles, it still remains 85% of the full capacity and the average conversion rate reaches 87.9%. The honeycombs maintain good structural integrity, shown in Figure S6, Supporting Information. Despite the excellent stability performed by the honeycomb units, more multicycle tests with larger scales of $(Mn_{0.8}Fe_{0.2})_2O_3$ are still needed in future studies. There is also room to further promote the thermal shock resistance and heat transfer characteristics of the porous $(Mn_{0.8}Fe_{0.2})_2O_3$ unit with novel structure design and doping strategies.

2.2. Microstructural Evolution

To elucidate the underlying reasons for exceptional reaction performance of the $(Mn_{0.8}Fe_{0.2})_2O_3$ material, various physical and chemical characterization techniques are employed to investigate the redox process and reaction pathways as shown in **Figures 3–5**. Figure 3a shows the XRD patterns of the

ADVANCED
SCIENCE NEWS
www.advancedsciencenews.com

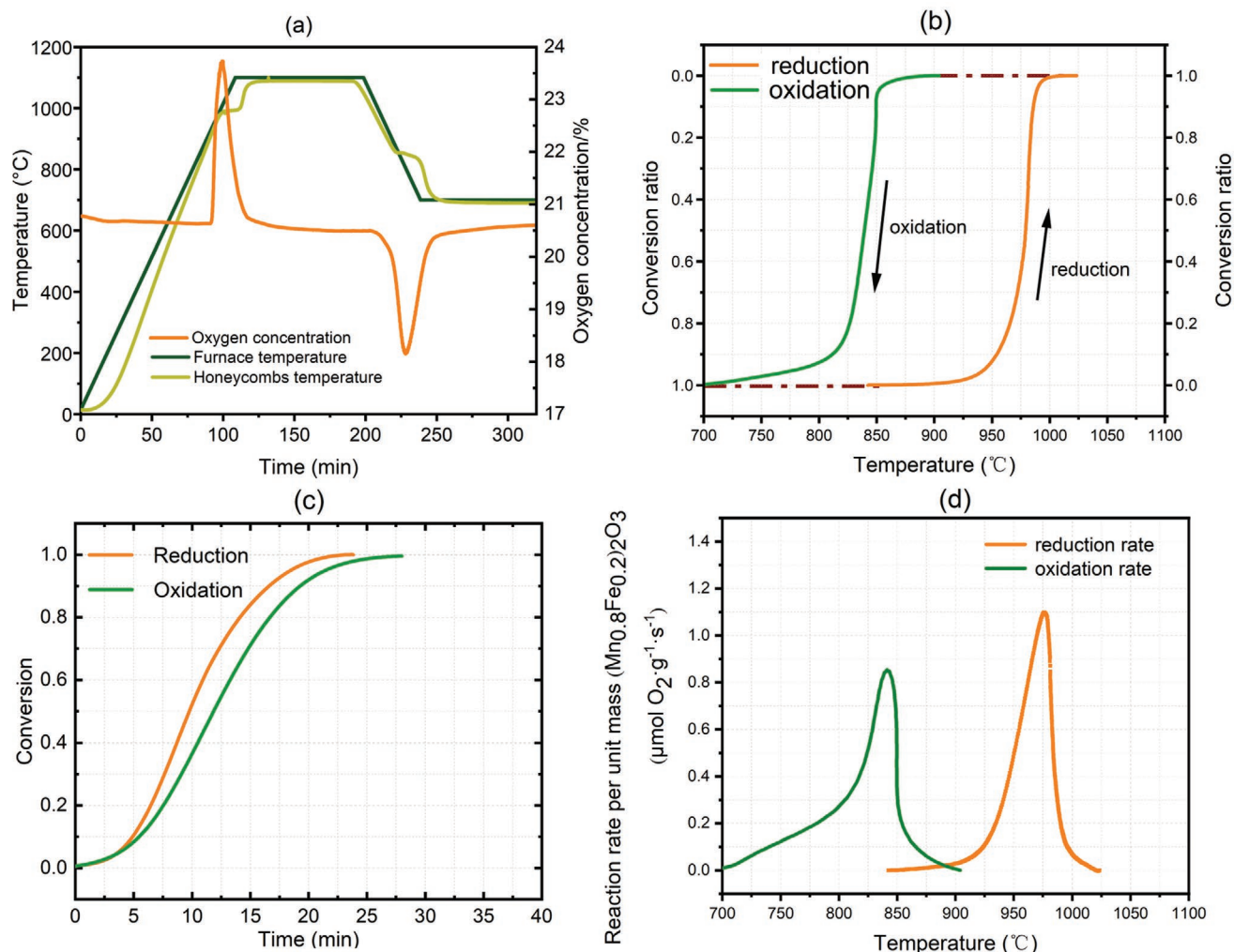NANO · MICRO
small
www.small-journal.com

Figure 1. a) Oxygen concentration and temperature variation curve, b) conversion curves varied with temperature, c) conversion rate curves, and d) reaction rate curves.

$(Mn_{0.8}Fe_{0.2})_2O_3$ at different stages (after synthesis, after reduction step, and after re-oxidation). The synthesized sample exhibits distinct reflections of $(Mn, Fe)_2O_3$ (bixbyite, ICCD 00-041-1442), indicating a uniform formation of continuous solid solution. However, polymorphic phases were observed in the reduced sample as shown in Figure 3b. A clear shift of the reflections to lower 2θ was observed after reduction, presenting a mixed phase with the main tetragonal spinel (Hausmannite, $Mn_{2.7}Fe_{0.3}O_4$, ICCD 04-005-9817) and minor cubic spinel (Jacobsite, $MnFe_2O_4$, ICCD 01-073-1964). The crystal constants of these two phases are shown in Table S1, Supporting Information. The shift to lower 2θ indicates more Mn ions were substituted by Fe ions with a smaller ionic radius. It could be also observed that Fe incorporation condenses the crystal cell along c axes, leading to a transition from tetragonal spinel to cubic spinel. Carrillo[27,30] attributed the enhancement of reaction performance after Fe doping to the easier transition of the cubic jacobsite to the cubic bixbyite in a view of structural similarity. To further probe the phase transformation, $(Mn_{0.33}Fe_{0.67})_2O_3$ and $MnFe_2O_4$ were synthesized using sol-gel method and self-propagating combustion. Both the

$(Mn_{0.33}Fe_{0.67})_2O_3$ and the $MnFe_2O_4$ went through the same reaction process as $(Mn_{0.8}Fe_{0.2})_2O_3$ did, and related XRD patterns are shown in Figure S7a, S7b, Supporting Information. Separate bixbyite and hematite phases (Fe_2O_3, ICDD 01-089-0599) in $(Mn_{0.33}Fe_{0.67})_2O_3$ were observed before reaction, then only the jacobsite ($MnFe_2O_4$) phase remains after reduction, and again cubic Mn_2O_3 (bixbyite) and tetragonal Fe_2O_3 (hematite) were observed after $MnFe_2O_4$ oxidation. But no significant change was observed in the further reduction of $MnFe_2O_4$, which agrees with the reported Fe−Mn−O phase diagrams,[31] as shown in Figure S8, Supporting Information. The segregation of hematite phase occurs when $0.45 < x(Fe) < 0.6$. As shown in Figure S9, Supporting Information, the reaction activity and enthalpy of $(Mn_{0.33}Fe_{0.67})_2O_3$ was not as good as $(Mn_{0.8}Fe_{0.2})_2O_3$. Indeed, an excessive Fe incorporation is indicated during the oxidation process when the single jacobsite phase transforms into cubic bixbyite and tetragonal hematite. To reach the best performance of $(Mn_{0.8}Fe_{0.2})_2O_3$ in the oxidation process, a mere transition from the cubic jacobsite to the cubic bixbyite is not enough. Instead, a joint transition from the cubic jacobsite and tetragonal hausmannite to bixbyite is needed.
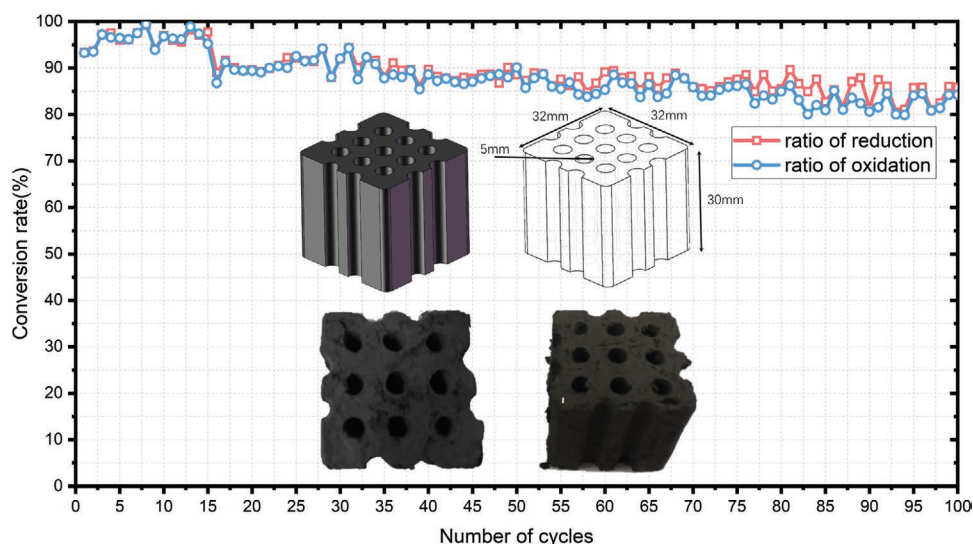
ADVANCED
SCIENCE NEWS

www.advancedsciencenews.com

NANO · MICRO
small
www.small-journal.com

Figure 2. The reduction and oxidation ratio of 100 cycles. The honeycombs gone through a complete reduction-oxidation process was regarded as a cycle. The red represents the reaction ratio of every reduction process, and the blue represents every oxidation.
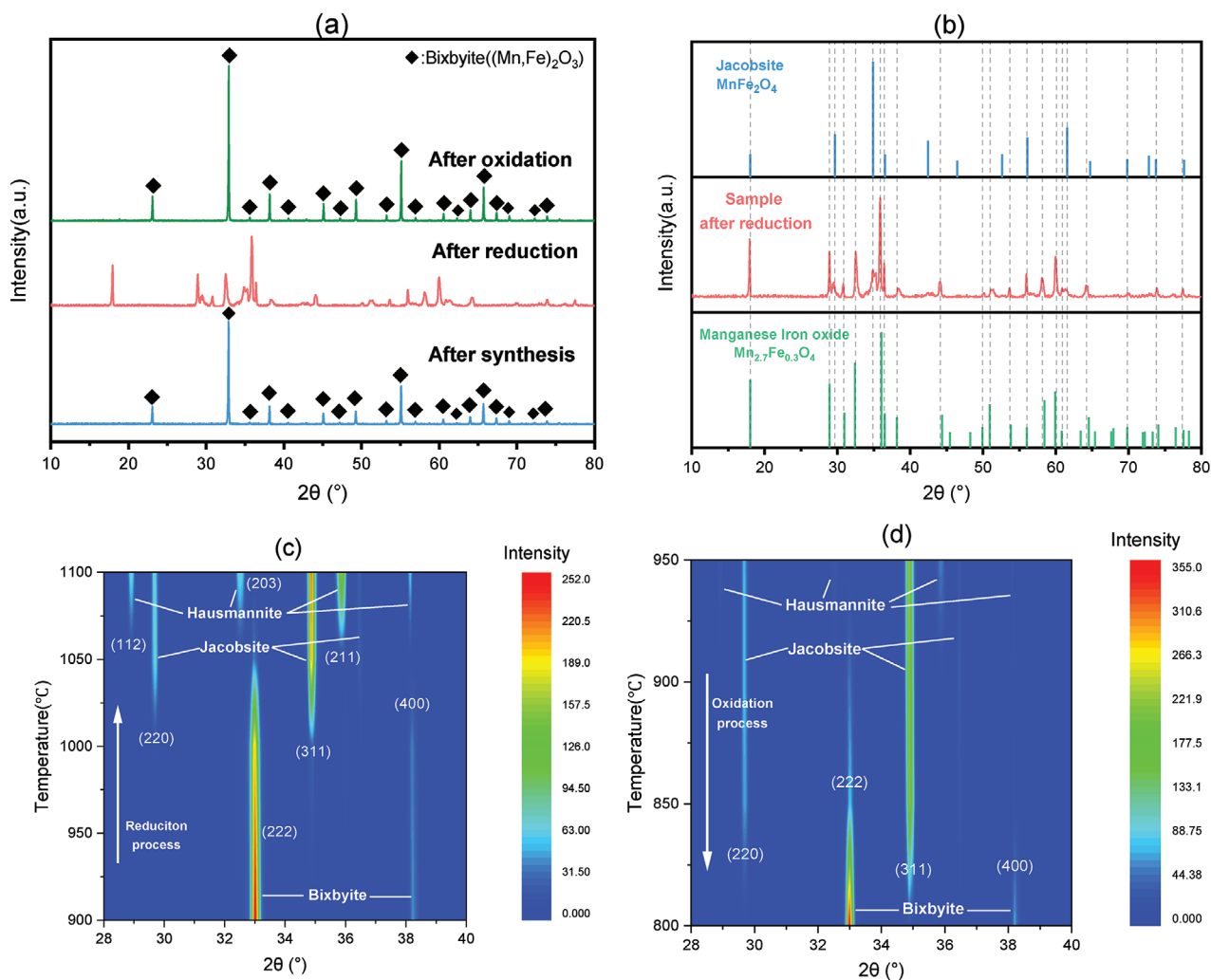

Figure 3. a) XRD patterns of the $(Mn_{0.8}Fe_{0.2})_2O_3$ at different stages, b) more clarity XRD patterns of the $(Mn_{0.8}Fe_{0.2})_2O_3$ after reduction, c) in situ XRD contour plots of reduction process, and d) in situ XRD contour plots of the oxidation process.
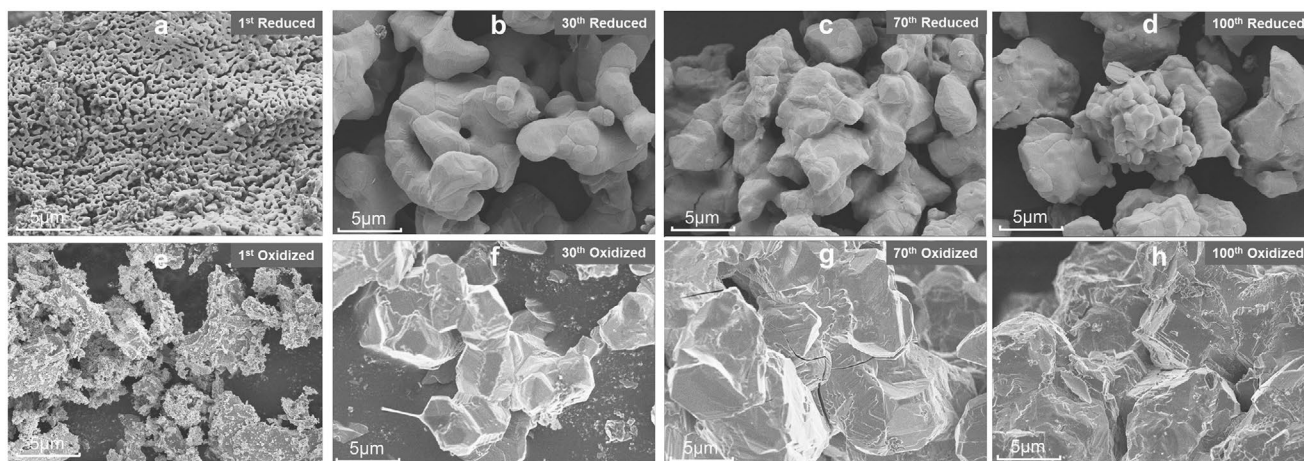
Figure 4. Representative SEM images of the $(Mn_{0.8}Fe_{0.2})_2O_3$ at different stages after redox cycling: a–d) Reduced sample after 1st, 30th, 70th, and 100th cycle, e–h) Oxidized sample after 1st, 30th, 70th, and 100th cycle

To further investigate the crystal phase transition during the redox reaction, the in situ XRD technique was employed with the same reaction conditions as in the TGA experiment. In situ XRD contour plots of both the reduction and oxidation processes are presented as shown in Figure 3c,3d. In the reduction process, the jacobsite first emerges when the temperature rises to 1000 °C, with the intensity of bixbyite fading away. Then the hausmannite appears at a higher temperature (>1050 °C), indicating the phase transition occurs after the formation of the jacobsite in the reduction. In the oxidation process, the hausmannite transforms to the bixbyite before the jacobsite fades away. It can thus be concluded that the synergetic effect of the hausmannite and the jacobsite is the cause of the performance improvement after Fe incorporation.

The morphological and structural evolution of the $(Mn_{0.8}Fe_{0.2})_2O_3$ is observed via the SEM analysis, where the representative images at different stages after the redox cycling are presented as shown in **Figure 4**. In the first cycle, the reduced and oxidized samples exhibit continuous reticular porous structure and flocculent cotton-like structure as shown in Figure 4a, 4e. As observed in Figure 4b, 4f, the grain sizes grow quickly after 30 redox cycles due to the fusion of large grains in oxidation and the merge of small grains into the large grains, which is driven by the surface energy differences of different grain sizes (Ostwald ripening).[32] However, the grain size in reduced samples keeps close after 30 cycles, because dispersive little grains are generated from the cleaving of large grains due to the release of oxygen in the reduction process. In this way, the material densification that happens in the oxidation is eliminated by the oxygen-release effect in the reduction, enabling effective oxygen diffusion in the next cycles. This phenomenon is also consistent with the multicycle conversion rates as given in Figure 2, where a stable performance is observed after 30 cycles.

Scanning transmission electron microscopy combined with energy-dispersive spectrometer (STEM-EDS) and High-resolution transmission electron microscopy (HRTEM) techniques are further employed to investigate the element distribution and the $(Mn_{0.8}Fe_{0.2})_2O_3$ structure as shown in

Figure 5. For the as-synthesized sample, a homogeneous distribution of Mn and Fe is observed through the STEM-EDS mapping (Figure 5a). The corresponding HRTEM images exhibit well-resolved lattice fringes of 2.72Å, which can be ascribed to (Mn, Fe)$_2$O$_3$ (222) facet, confirming a complete mixture of Mn and Fe in the as-synthesized sample. However, the STEM-EDS mapping of the $(Mn_{0.8}Fe_{0.2})_2O_3$ after reduction exhibits distinct core-shell structure as shown in Figure 5b, where Fe-rich and Fe-poor areas are observed in the core region and the shell region, respectively. The HRTEM images of core and shell also exhibit clear lattice fringes of 4.90 and 2.49Å, corresponding to $MnFe_2O_4$ (111) and $Mn_{2.7}Fe_{0.3}O_4$ (211) facets, respectively. More elemental-mapping results are shown in Figure S10, Supporting Information. These results provide clear evidence that the Fe element is incorporated into the Mn_3O_4 lattice, resulting in the core-$MnFe_2O_4$ (jacobsite) and shell-$Mn_{2.7}Fe_{0.3}O_4$ (Hausmannite). It seems Fe migrates into the inner lattice during the reduction process and results in the formation of core-shell structure. In contrast, the STEM-EDS mapping of the $(Mn_{0.8}Fe_{0.2})_2O_3$ after oxidation shows a homogeneous distribution of Mn and Fe with the lattice fringes to be 4.71 and 2.71Å (Figure 5c), corresponding to (Mn, Fe)$_2$O$_3$ (200) and (Mn, Fe)$_2$O$_3$ (222) facets, respectively. This implies the regeneration of (Mn, Fe)$_2$O$_3$ with the Fe element migrating outward from the core $MnFe_2O_4$. These results show a clear crystalline phase evolution of the $(Mn_{0.8}Fe_{0.2})_2O_3$ in the redox reaction process. Core-shell $MnFe_2O_4@Mn_{2.7}Fe_{0.3}O_4$ structure is formed from the uniformly distributed bixbyite after reduction, which is probably the decisive factor in improving the oxidation performance.

2.3. Surface Chemistry

The evolution of the surface Fe and O species of the $(Mn_{0.8}Fe_{0.2})_2O_3$ is probed using the X-ray photoelectron spectroscopy (XPS), where the Fe 2p spectra of the material at different stages are compared as shown in **Figure 6**a. The as-synthesized powder shows a strong peak at 710.9 eV and a satellite peak at 718.9 eV, which is assigned to the Fe^{3+},
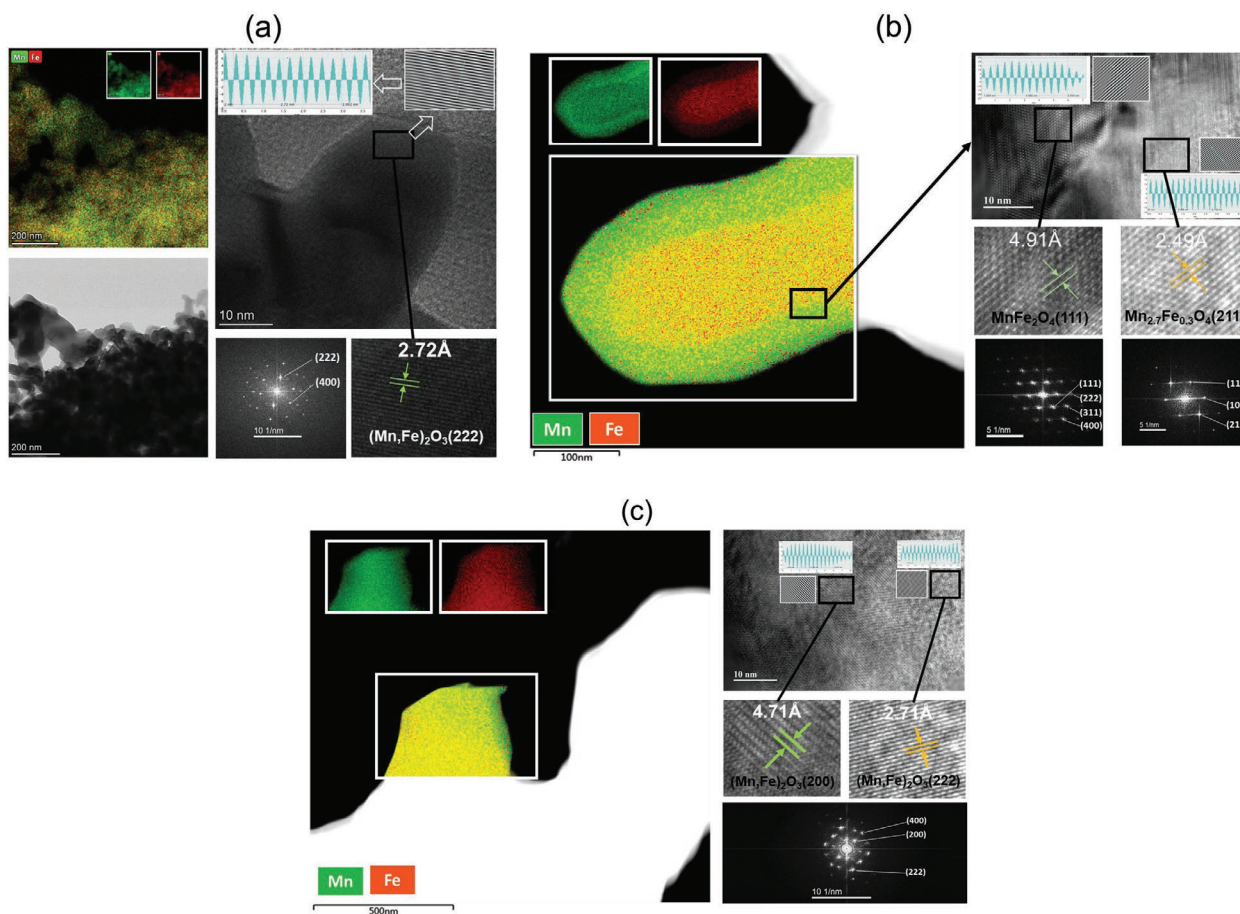
Figure 5. HRTEM images and corresponding element-mapping images of the $(Mn_{0.8}Fe_{0.2})_2O_3$ at different stages: a) as-synthesized, b) after reduction, and c) after oxidation.
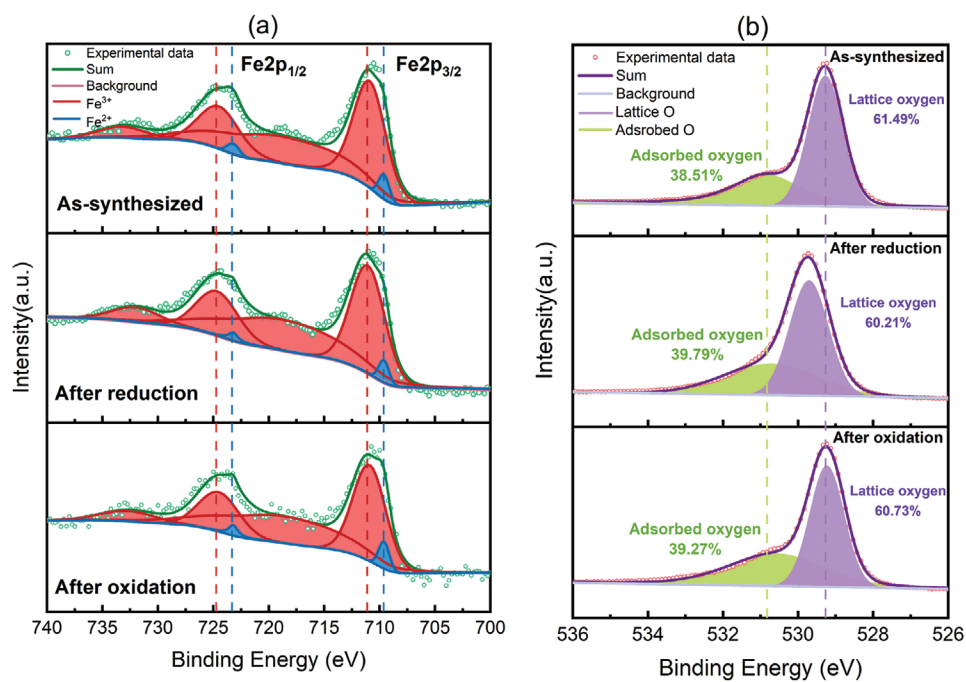

Figure 6. a) Fe 2p XPS spectra of the $(Mn_{0.8}Fe_{0.2})_2O_3$ at different stages, b) O 1s XPS spectra of the $(Mn_{0.8}Fe_{0.2})_2O_3$ at different stages.

indicating the surface Fe is mainly the bixbyite. However, the Fe species is still predominantly the trivalent ion after the reduction and oxidation, indicating that the surface Fe is probably not involved in the redox reaction. Two distinct components are further observed in the deconvolution O 1s spectra as shown in Figure 6b. The predominant one between 529 and 530 eV agrees well with the signature of lattice oxygen, and the minor one at 530.8 eV is in accordance with the signature of adsorbed oxygen, including O_2 and hydroxyls of H_2O. The proportion of the lattice/adsorbed oxygen in the $(Mn_{0.8}Fe_{0.2})_2O_3$ remains constant during the redox process. Compared with Mn_2O_3, the proportion of adsorbed oxygen decreases from 52.29 to 38.51% (Figure S11, Supporting Information), evidencing that part of the adsorbed O transforms into the Lattice O on the surface after iron doping. It should be noted that the enhancement of lattice oxygen release and adsorption is the rate-determining step in the redox cycles.[33] Hence, it is reasonable to speculate that the increase of surface lattice oxygen results in the increase of active lattice oxygen and its migration enhancement into the oxygen vacancy, which facilitates the reaction activity and conversion rate in the oxidation process.

2.4. Redox Mechanism

To build a solid understanding about the performance of the observed core-shell material, DFT calculations are conducted to investigate the oxidation reaction path, which associates with oxygen adsorption/dissociation and oxygen ion migration within the lattice. Different slab models are adopted to find out the most stable surface with the lowest surface energy as listed in Table S2, Supporting Information. The surface energy of $Mn_{2.7}Fe_{0.3}O_4$ is much lower than $MnFe_2O_4$, favoring the formation of the core-shell structure with the $Mn_{2.7}Fe_{0.3}O_4$ enfolding the $MnFe_2O_4$ during the crystal growth.[34] The oxygen adsorption and dissociation in the oxidation were studied on the interfaces of metal oxides. As shown in **Figure 7**a, the $Mn_3O_4(100)$ has the highest adsorption (–1.06 eV) and dissociation energies (–1.42 eV) with the largest reaction barrier (0.92 eV). $Mn_{2.7}Fe_{0.3}O_4(100)$ has a smaller reaction barrier (0.51 eV), but its energy change is negligible (–0.05 eV). $MnFe_2O_4(100)$ has the strongest oxygen adsorption intensity (–2.46 eV), the lowest energy barrier (0.15 eV), and the most significant energy change (–1.11 eV), illustrating the advantage of the shell and the core in the O_2 adsorption and dissociation processes, which is vital to the increase of reaction rates. The geometric structure diagrams of the adsorption and dissociation process are shown in Figure S12, Supporting Information.

To further study the diffusion of the oxygen ion within the lattice, the formation of oxygen vacancies $E(V_O)$ and the migration energy barriers of Mn_3O_4 and $Mn_{2.7}Fe_{0.3}O_4$ in the first and second atomic layers are calculated with Mn_3O_4 as the reference, as shown in Figure 7b, 7c. Detailed geometric structure diagrams of oxygen migration are shown in Figure S13, Supporting Information. The calculated results indicate that the $E(V_O)$ of $Mn_{2.7}Fe_{0.3}O_4(100)$ is significantly lower than those of $Mn_3O_4(100)$ and $MnFe_2O_4(100)$. In contrast to pure $Mn_3O_4(100)$ lattice, the oxygen anions (u2 and d2) are more

likely to be removed after replacing a Mn ion with a Fe ion within the $Mn_{2.7}Fe_{0.3}O_4(100)$ with the lowest $E(V_O)$ of 1.17 eV and 1.91 eV. However, the $E(V_O)$ of $MnFe_2O_4(100)$ is slightly lower than that of $Mn_3O_4(100)$. The lower formation energies of oxygen vacancies approaching the Fe cation in the lattice of $Mn_{2.7}Fe_{0.3}O_4(100)$ and $MnFe_2O_4(100)$ demonstrate that the Mn−O bond is weakened by Fe cation, and this effect is more significant in the shell than the core. The energy barriers of oxygen ion migration in three lattices from the first atomic layer to the third atomic layer are also presented. The energy barrier of $Mn_3O_4(100)$ reaches 3.23 eV, indicating that the oxygen diffusion is extremely difficult in its lattice, which corresponds to the slow oxidation rate as shown in Figure S2, Supporting Information. For comparison, $Mn_{2.7}Fe_{0.3}O_4(100)$ and $MnFe_2O_4(100)$ have obviously lower energy barriers (1.45 and 0.9 eV, respectively), indicating their stronger activity for oxygen ion migration. The oxidation products will accumulate on the surface of reduced material as the reaction progress. The oxygen will have to diffuse within the lattice of oxidized phase bixbyite when the surface is completely covered by oxidation products. Hence the DFT study for the formation energies of oxygen vacancies of $Mn_2O_3(110)$ and $(Mn_{0.8}Fe_{0.2})_2O_3(110)$ was carried out. As shown in Figure S14, Supporting Information, the $E(V_O)$ of $(Mn_{0.8}Fe_{0.2})_2O_3(110)$ is significantly lower than that of $Mn_2O_3(110)$ at the surface layer and slightly lower than that of $Mn_2O_3(110)$ at the second layer, indicating that the presence of Fe also facilitates the O anions diffusion within the product layer. Overall, DFT calculations show the introduction of the Fe cation can enhance the adsorption and dissociation of oxygen on the surface of reduced material and has a promotional effect on subsequent oxygen ion migration within the lattice.

Based on the experimental analyses and DFT calculations presented above, a potential reaction mechanism for the $(Mn_{0.8}Fe_{0.2})_2O_3$ in reduction and oxidation processes is depicted in **Figure 8**. In the reduction process, the atomic thermal motion causes the desorption of the surface lattice oxygen of the $(Mn_{0.8}Fe_{0.2})_2O_3$, which generates the gaseous oxygen, free electrons, and oxygen vacancies. Then the free electrons rapidly migrate inwards to break the Mn−O bond and drive more inner O ions to migrate towards the surface vacancies. Similar to the Wagner effect,[35] the formation of oxygen vacancy and the migration of electrons result in the electric potential difference between the surface and the inside, driving the Fe^{3+} cations to transport from the high-potential surface to the low-potential inside. As a result, the $Mn_{2.7}Fe_{0.3}O_4$ with a lower surface energy tends to enfold the $MnFe_2O_4$, forming the self-assembled core-shell $MnFe_2O_4@Mn_{2.7}Fe_{0.3}O_4$ structure in the growth of the crystal. In the oxidation process, the oxygen is adsorbed and dissociated into O ions, which migrate to the surface oxygen vacancies and into the inner lattice of the shell and the core in turn. In the meanwhile, the electrons of Mn cations migrate from the inner lattice to the surface and combine with the oxygen ions, which lead to a reversed electric field compared with the reduction process and drives the Fe^{3+} cations to move towards the outside surface and form a homogeneous structure.

Overall, the phase transformation between the core-shell structure (hausmannite-jacobsite) and homogenous structure
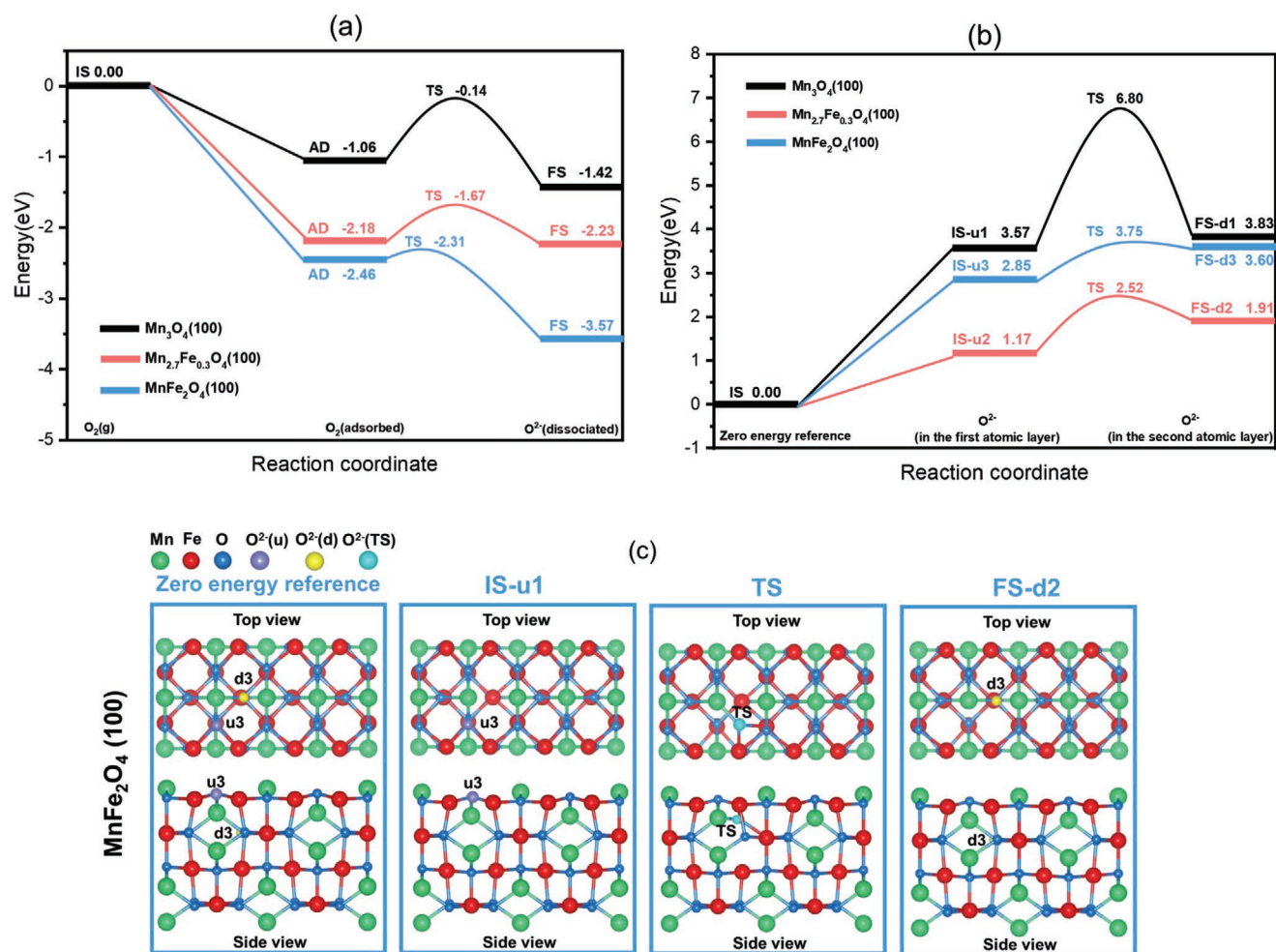
**ADVANCED
SCIENCE NEWS**

www.advancedsciencenews.com

NANO · MICRO

small

www.small-journal.com

Figure 7. DFT calculations results. a) Potential energy diagrams for oxygen adsorption and dissociation on the surface of $Mn_3O_4(100)$, $Mn_{2.7}Fe_{0.3}O_4(100)$, $MnFe_2O_4(100)$. b) The formation energies of oxygen vacancies $E(V_O)$ at different sites of $Mn_3O_4(100)$, $Mn_{2.7}Fe_{0.3}O_4(100)$, and $MnFe_2O_4(100)$ and energy barriers of migration. c) Representative top and side view of geometric structures of $MnFe_2O_4(100)$ at different states during migration. The zero-energy reference in Figure 7b, 7c corresponds to the sum of energies of the oxygen molecule and clean surface, complete surface without oxygen vacancy respectively. The oxygen anions in the first atomic layer are labeled with "u" and the oxygen in the second atomic layer is labeled with "d". The migration was the process that $O^{2-}(u)$ migrated to the vacancy that $O^{2-}(d)$ occupied.

(bixbyite) can proceed reversibly with the enhanced lattice oxygen adsorption and transportation through Fe doping, which is supported by the XRD, the in situ XRD, and the electron microscopy (STEM-EDS, HRTEM) characterizations. DFT calculations further demonstrate the intensity increase of $Mn_{2.7}Fe_{0.3}O_4$ and $MnFe_2O_4$ surfaces in the oxygen adsorption and dissociation during the oxidation process. As a result, the synergistic effects of the enhanced oxygen diffusion through Fe incorporation and the reversible evolution between the core-shell and the homogeneous structure enable the highly efficient solar TCES in reversibly redox cycles.

3. Conclusions

Bixbyite-type $(Mn_{0.8}Fe_{0.2})_2O_3$ is synthesized and extruded into honeycomb units for practical TCES applications. Compared with the powder-Mn_2O_3 that has only a 58% conversion rate in the first redox cycle, the powder-$(Mn_{0.8}Fe_{0.2})_2O_3$ shows a 96.69% conversion rate over 10 cycles, and the honeycomb-$(Mn_{0.8}Fe_{0.2})_2O_3$ maintained >85% conversion rate over 100 redox cycles. Such a superior performance is highly related to the oxygen diffusion rate both on the surface and in the lattice. Due to the increased active sites provided by the self-assembled core-shell $MnFe_2O_4@$ $Mn_{2.7}Fe_{0.3}O_4$ structure, the oxygen adsorption and dissociation processes are enhanced on both the core and the shell. The increased oxygen diffusion rate within the lattice attributes to the presence of Fe, which weakens the Mn—O bond. As a result, the energy barrier is reduced and the reaction activity is improved. The phase transformation between core-shell structure of jacobsite ($MnFe_2O_4$)-hausmannite ($Mn_{2.7}Fe_{0.3}O_4$) and homogenous structure of bixbyite solid solution $(Mn_{0.8}Fe_{0.2})_2O_3$ promoted the reversibility for TCES. These results will provide a fundamental understanding of self-assembled core-shell structure evolution and serve as guidelines towards the rational design of advanced materials for the solar TCES.
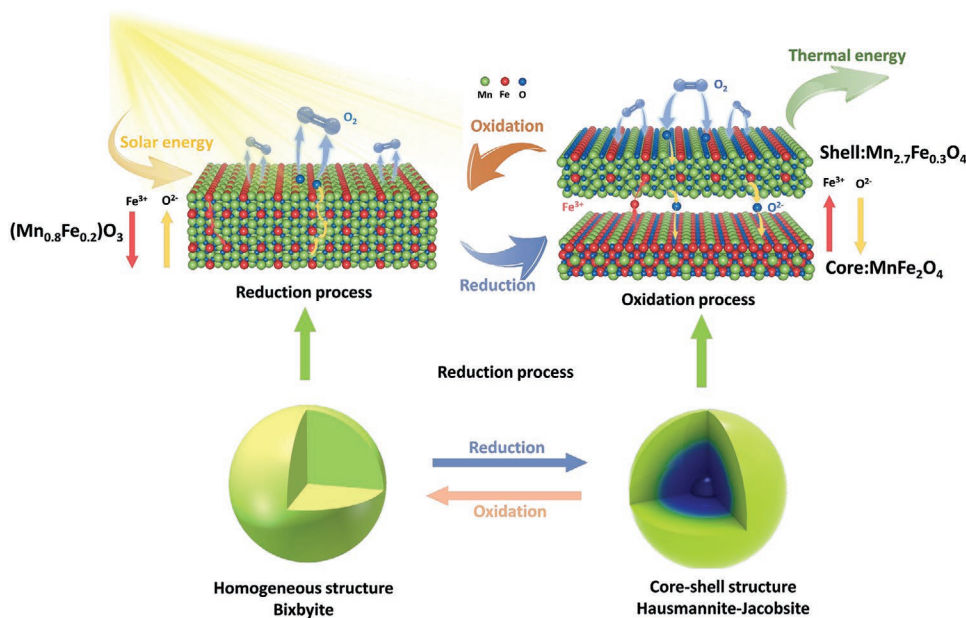
Figure 8. Schematic representation of the proposed reaction mechanism for reduction and oxidation processes of the $(Mn_{0.8}Fe_{0.2})_2O_3$.

4. Experimental Section

Materials Synthesis: The bixbyite-type $(Mn_{1-\delta}Fe_\delta)_2O_3$ was synthesized by citrate sol-gel method. Manganous nitrates, citric acid, and ethylene glycol were used in an aqueous solution. The molar ratios of Fe and Mn were set as 0:1, 1:9, 2:8, 3:7, 4:6, and 2:1 to prepare the mixed oxides with different doping ratios. The gelatinous mixture was calcined for 2 and 4 h at 200 and 800 °C, respectively, to eliminate the nitric oxide and ensure the formation of the bixbyite crystal structure. Bixbyite-type Mn_2O_3 with Fe doping of 10, 20, 30, and 40 mol% were prepared, tagged as $(Mn_{0.9}Fe_{0.1})_2O_3$, $(Mn_{0.8}Fe_{0.2})_2O_3$, $(Mn_{0.7}Fe_{0.3})_2O_3$, and $(Mn_{0.6}Fe_{0.4})_2O_3$, respectively. In addition, Mn_2O_3 with Fe doping of 66.7 mol% was tagged as $(Mn_{0.33}Fe_{0.67})_2O_3$. $MnFe_2O_4$ was synthesized via a self-propagating combustion method; a detailed description was shown in Supporting Information. Commercial Mn_2O_3 (Sinopharm) powder was referred to as the control group. To further investigate the reaction activity and stability in a hundred-gram scale with porous structure, the synthesized powder was extruded into cubic honeycombs via a mold with the side length and height to be 32 and 30 mm, respectively. The 20 wt% polyvinyl alcohol (PVA) solution was used as a binder for the powder glued together. These honeycombs were calcined at 700 °C for 4 h to harden the structure.

Redox Reactivity: The redox activities of the materials were investigated in both the powder and the honeycomb units. The redox reactivity tests of the powders were first carried out in a Netzsch STA 449 Jupiter F3 simultaneous thermal analyzer at air atmosphere with a 50 mL min^{-1} gas flow rate. Air was used in the whole process to be consistent with the real situation in CSP. For isokinetic TGA measurements, the materials were measured with a constant ramp rate of 5, 10, and 20 °C min^{-1} between 600 and 1100 °C. For the subsequent material characterization, more powders were prepared with a 100 mL min^{-1} air flow rate with the same thermal process. A test bench was built to study the reaction activities of the materials with honeycomb structure as shown in Figure S15, Supporting Information. An alundum tube was used as the reaction vessel to accommodate the honeycombs. Two thermocouples were tied to holes of the honeycomb, where the measured average temperature was regarded as the material temperature. The alundum tube was heated by the furnace to 1100 °C with a 10 °C min^{-1} heating/cooling rate. The reactant gas, air, was provided by an air compressor and passed an Omega mass flowmeter to keep a constant flow rate of 10L min^{-1}.

The exit was divided into two bypasses, one directly discharged the gas to atmosphere while another was connected to a Signal paramagnetic oxygen analyzer to record the oxygen concentration variation.

Material Characterization: The materials were characterized at various stages (after synthesis, after reduction, after re-oxidation, and after multicycle reactive tests) via physical and chemical techniques. The XRD analysis was performed with a PANalytical B.V. (Netherland) X-pert Powder diffractometer (Cu Kα radiation) in the diffraction angle (2θ) range of 10–80° with a step of 0.02° and 30 s counting time per angle. The crystal phases were identified by using the ICDD PDF-4 database. The in situ XRD analysis was used to study the crystal phase transition during the redox cycle via a SmartLab instrument. XPS was employed to study the surface ion valency and concentration via a Thermo Scientific K-Alpha instrument. The analysis of SEM was carried out via a SU8010 field-emission scanning electron microscope to observe the microstructure and morphology of the materials before and after redox cycles. HRTEM and STEM-EDS were employed to identify the crystallinity, morphology, and elemental distribution and composition of samples after different processes. These measurements were carried out on a Tecnai G2 F20 S-TWIN microscope operated at 200 kV with a linear resolution of 0.14 nm.

Computation Details and Model Development: All the spin-polarized DFT calculations were carried out using the Vienna Ab-initio Simulation Package (VASP).[36,37] The projected-augmented wave (PAW) pseudopotentials were utilized to describe the core electrons, and plane-wave basis sets with a kinetic energy cutoff of 500 eV were adopted to treat the valence electrons. The Perdew–Burke–Ernzerhof (PBE) exchange-correlation functional of the generalized gradient approximation (GGA) was used.[38] The k-point sampling was performed using the Monkhorst–Pack scheme with meshes for the bulk and surfaces as given in Table S3, Supporting Information. The DFT + U method was used to treat the on-site Coulomb and exchange interactions of highly localized states in the d or f orbitals of the metal oxides. Effective U_{Mn} = 2.0 eV and U_{Fe} = 4.5 eV were used for both the 3d orbital of Mn and Fe in metal oxides, respectively, which is consistent with previous values used by Jacobsite.[39] All the structures were relaxed until the forces on each ion were less than 0.02 eV Å, and the convergence criterion for the energy was set as 10^{-5} eV. The climbing image nudged elastic band (CI-NEB) combined with minimum-mode following dimer method was used to locate the transition state structure of the reaction.

All the transition state structures were identified by vibrational analysis. To study the oxidation process of the $(Mn_{0.8}Fe_{0.2})_2O_3$, five surface models of $MnFe_2O_4(100)$, $Mn_3O_4(100)$, $Mn_{2.7}Fe_{0.3}O_4(100)$, $Mn_2O_3(110)$, and $(Mn_{0.8}Fe_{0.2})_2O_3(110)$ were used. The explicit surface structures are presented in Table S2, Supporting Information. The optimized lattice constants of the metal oxides are listed in Table S4, Supporting Information. The typical low-index surface $MnFe_2O_4$ (100) was used to investigate the O_2 adsorption, dissociation, and O anion migrations. The Mn-terminated surface was more stable than the Fe-terminated due to the lower surface energy.[40,41] $MnFe_2O_4$ (100) was modeled as a nine atomic layer slab. The Mn_3O_4 (100) and $Mn_{2.7}Fe_{0.3}O_4$ (100) were also used to investigate the O_2 adsorption, dissociation, and O anion migrations. The $Mn_2O_3(110)$ and $(Mn_{0.8}Fe_{0.2})_2O_3(110)$ were used to study the oxygen vacancy formation of oxidation products. Detailed structural parameters concerning the size of supercells, the number of atomic layers, and the vacuum space of surface slabs are provided in Table S5, Supporting Information.

Supporting Information

Supporting Information is available from the Wiley Online Library or from the author.

Conflict of Interest

The authors declare no conflict of interest.

Data Availability Statement

The data that support the findings of this study are available from the corresponding author upon reasonable request.

[1] A. J. Carrillo, J. Gonzalez-Aguilar, M. Romero, J. M. Coronado, *Chem. Rev.* **2019**, *119*, 4777.
[2] A. Dreos, Z. Wang, J. Udmark, A. Ström, P. Erhart, K. Börjesson, M. B. Nielsen, K. Moth-Poulsen, *Adv. Energy Mater.* **2018**, *8*, 1703401.
[3] S. Ströhle, A. Haselbacher, Z. R. Jovanovic, A. Steinfeld, *Energy Environ. Sci.* **2016**, *9*, 1375.
[4] C. Agrafiotis, M. Roeb, C. Sattler, *Sol. Energy* **2016**, *139*, 695.
[5] C. Agrafiotis, T. Block, M. Senholdt, S. Tescari, M. Roeb, C. Sattler, *Sol. Energy* **2017**, *149*, 227.
[6] C. Agrafiotis, A. Becker, M. Roeb, C. Sattler, *Sol. Energy* **2016**, *139*, 676.
[7] A. J. Schrader, G. De Dominicis, G. L. Schieber, P. G. Loutzenhiser, *Sol. Energy* **2017**, *150*, 584.
[8] T. Block, M. Schmücker, *Sol. Energy* **2016**, *126*, 195.
[9] M. Deutsch, F. Horvath, C. Knoll, D. Lager, C. Gierl-Mayer, P. Weinberger, F. Winter, *Energy Fuels* **2017**, *31*, 2324.
[10] A. Singh, S. Tescari, G. Lantin, C. Agrafiotis, M. Roeb, C. Sattler, *Sol. Energy* **2017**, *144*, 453.
[11] C. Pagkoura, G. Karagiannakis, A. Zygogianni, S. Lorentzou, M. Kostoglou, A. G. Konstandopoulos, M. Rattenburry, J. W. Woodhead, *Sol. Energy* **2014**, *108*, 146.
[12] C. Pagkoura, G. Karagiannakis, A. Zygogianni, S. Lorentzou, A. G. Konstandopoulos, *Energy Procedia* **2015**, *69*, 978.
[13] D. Müller, C. Knoll, W. Artner, M. Harasek, C. Gierl-Mayer, J. M. Welch, A. Werner, P. Weinberger, *Sol. Energy* **2017**, *153*, 11.
[14] G. Karagiannakis, C. Pagkoura, E. Halevas, P. Baltzopoulou, A. G. Konstandopoulos, *Sol. Energy* **2016**, *133*, 394.
[15] L. André, S. Abanades, L. Cassayre, *J. Solid State Chem.* **2017**, *253*, 6.
[16] C. Agrafiotis, S. Tescari, M. Roeb, M. Schmücker, C. Sattler, *Sol. Energy* **2015**, *114*, 459.
[17] S. Tescari, A. Singh, C. Agrafiotis, L. de Oliveira, S. Breuer, B. Schlögl-Knothe, M. Roeb, C. Sattler, *Appl. Energy* **2017**, *189*, 66.
[18] E. Alonso, C. Pérez-Rábago, J. Licurgo, E. Fuentealba, C. A. Estrada, *Sol. Energy* **2015**, *115*, 297.
[19] M. Jafarian, M. Arjomandi, G. J. Nathan, *Appl. Energy* **2017**, *201*, 69.
[20] I. A. Al-Shankiti, B. D. Ehrhart, B. J. Ward, A. Bayon, M. A. Wallace, R. Bader, P. Kreider, A. W. Weimer, *Sol. Energy* **2019**, *183*, 17.
[21] M. Hamidi, A. Bayon, V. M. Wheeler, P. Kreider, M. A. Wallace, T. Tsuzuki, K. Catchpole, A. W. Weimer, *Chem. Eng. Sci.* **2019**, *201*, 74.
[22] A. J. Carrillo, D. P. Serrano, P. Pizarro, J. M. Coronado, *J. Energy Storage* **2016**, *5*, 169.
[23] B. Wong, Thermochemical heat storage for concentrated solar power. Final Report for the US Department of Energy, **2011**, https://doi.org/10.2172/1039304.
[24] A. J. Carrillo, D. P. Serrano, P. Pizarro, J. M. Coronado, *J. Mater. Chem. A* **2014**, *2*, 19435.
[25] M. Wokon, A. Kohzer, M. Linder, *Sol. Energy* **2017**, *153*, 200.
[26] M. Wokon, T. Block, S. Nicolai, M. Linder, M. Schmücker, *Sol. Energy* **2017**, *153*, 471.
[27] A. J. Carrillo, D. P. Serrano, P. Pizarro, J. M. Coronado, *ChemSusChem* **2015**, *8*, 1947.
[28] A. J. Carrillo, J. Moya, A. Bayón, P. Jana, V. A. de la Peña O'Shea, M. Romero, J. Gonzalez-Aguilar, D. P. Serrano, P. Pizarro, J. M. Coronado, *Sol. Energy Mater. Sol. Cells* **2014**, *123*, 47.
[29] N. W. Hlongwa, D. Sastre, E. Iwuoha, A. J. Carrillo, C. Ikpo, D. P. Serrano, P. Pizarro, J. M. Coronado, *Solid State Ionics* **2018**, *320*, 316.
[30] A. J. Carrillo, D. P. Serrano, P. Pizarro, J. M. Coronado, *J. Phys. Chem. C* **2016**, *120*, 27800.
[31] J. V. Crum, B. J. Riley, J. D. Vienna, *J. Am. Ceram. Soc.* **2009**, *92*, 2378.
[32] T. Sugimoto, *J. Colloid Interface Sci.* **1978**, *63*, 16.
[33] Z. Zhang, J. Yu, J. Zhang, Q. Ge, H. Xu, F. Dallmann, R. Dittmeyer, J. Sun, *Chem. Sci.* **2018**, *9*, 3386.
[34] J. Szekely, J. W. Evans, H. Y. Sohn, *Gas-solid Reactions*, Academic Press **1976**, pp. 248–337, https://doi.org/10.1016/B978-0-12-680850-6.50012-3.
[35] C. Wagner, *Z. Phys. Chem.* **1933**, *21B*, 25.
[36] G. Kresse, J. Furthmüller, *Phys. Rev. B: Condens. Matter Mater. Phys.* **1996**, *54*, 11169.
[37] G. Kresse, J. Hafner, *Phys. Rev. B: Condens. Matter Mater. Phys.* **1994**, *49*, 14251.
[38] K. Burke, J. P. Perdew, M. Ernzerhof, *Phys. Rev. Lett.* **1996**, *77*, 3865.
[39] J.-R. Huang, C. Cheng, *J. Appl. Phys.* **2013**, *113*, 033912.
[40] Y. Yang, J. Liu, B. Zhang, F. Liu, *Chem. Eng. J.* **2017**, *308*, 897.
[41] Y. Hu, C. Zhao, L. Yin, T. Wen, Y. Yang, Y. Ai, X. Wang, *Chem. Eng. J.* **2018**, *349*, 347.